A 3μm difference frequency laser source for probing hydrocarbon plasmas

J H van Helden, G Hancock, R Peverall, G a D Ritchie

To cite this version:

J H van Helden, G Hancock, R Peverall, G a D Ritchie. A 3μm difference frequency laser source for probing hydrocarbon plasmas. Journal of Physics D: Applied Physics, 2011, 44 (12), pp.125202. ⟨10.1088/0022-3727/44/12/125202⟩. ⟨hal-00604887⟩

HAL Id: hal-00604887
https://hal.science/hal-00604887v1

Submitted on 30 Jun 2011

A 3 μm difference frequency laser source for probing hydrocarbon plasmas

J H van Helden, G Hancock, R Peverall and G A D Ritchie

Department of Chemistry, Physical and Theoretical Chemistry Laboratory,
University of Oxford, South Parks Road, Oxford OX1 3QZ, United Kingdom

E-mail: `robert.peverall@chem.ox.ac.uk`

Abstract. The practicality of a compact solid-state laser based difference frequency generation (DFG) system is demonstrated as a tool for probing hydrocarbon based plasmas. The laser light of a cw Nd:YAG operating at 1064 nm and one of two DFB diode lasers operating at 1560 nm and 1620 nm were mixed in a periodically poled lithium niobate (PPLN) crystal producing mid-infrared radiation at 3.35 μm and 3.1 μm for the detection of CH_4 and C_2H_6 at the first wavelength and C_2H_2 and C_2H_4 at the latter. The radiation was used to probe a rf capacitively coupled CH_4 plasma for a matrix of conditions, varying power (< 180 W) and pressure (< 1 Torr) in both direct absorption spectroscopy and wavelength modulation spectroscopy (WMS) experiments to achieve relatively high sensitivities while retaining accurate spectral information in the form of linewidths. A minimum detectable absorption coefficient α_{min} of 2×10^{-5} cm^{-1} was achieved for direct absorption spectroscopy which corresponds to a minimum detectable density for CH_4 of 1.7×10^{12} cm^{-3} and an α_{min} value of 2×10^{-6} cm^{-1} was achieved for WMS measurements on C_2H_2. The depletion of CH_4 was measured to increase from 23% at 40 W to 40% at 180 W at a pressure of 0.84 Torr, and the depletion increased to 56% as the pressure decreases to 0.45 Torr.

1. Introduction

Tunable narrow band light sources in the mid-infrared (MIR) region (3 – 20 μm) for molecular absorption spectroscopy are highly desirable for fundamental and applied plasma research. In this region, tunable lead salt diode lasers have been the most popular devices for tunable diode laser absorption spectroscopy (TDLAS), because they offer relatively high spectral intensity, narrow bandwidth and continuous tunability over an absorption profile [1]. However, these lasers have the drawback that they require cryogenic cooling. Furthermore, cheap tunable narrow-band optical sources operating in the 3 μm region where many molecules of fundamental and applied interest have strong C–H, N–H or O–H vibrational transitions are not readily available. Quantum cascade lasers are rapidly becoming the radiation source of choice for working in the MIR above 4 μm and will continue to do so as their emission wavelengths and that of interband cascade lasers (ICLs) decrease towards the 3 μm region [2]. In the meantime, there is an alternative method for the production of MIR radiation via nonlinear optical processes utilising widely available room temperature sources in the near-infrared (NIR). These lasers have the same advantageous features as the lead salt diode lasers but without the necessity of cryogenic operation making their use much simpler and because of their importance to telecommunications are based on mature technology. The NIR lasers are mixed in a non-linear cystal via a process called difference frequency generation (DFG) to produce a beam in the MIR with optical qualities directly related to those of the source lasers. The advent of the reliable production of periodically poled materials for applications in nonlinear optics in combination with widely tunable sources, such as external cavity diode lasers (ECDL), means that transitions can be accessed over a relatively large spectral range at high resolution ($\lesssim$ 20 MHz). Primarily, periodically poled lithium niobate (PPLN) has been used either in a DFG or optical parametric oscillator arrangement to generate radiation in the MIR ($\sim$ 3 μm) for gas detection applications [3, 4, 5, 6, 7].

In this paper, the practicality of a compact solid-state laser based DFG system is demonstrated as a tool for probing hydrocarbon based plasmas. These plasmas are frequently used for the deposition of diamond-like carbon (DLC) thin films which have attracted attention for many years now because of their excellent mechanical and optical properties. DLC films are nowadays used as protective coatings on magnetic storage discs, optical elements, razor blades and car parts [8] and as an intermediate layer for liquid crystal alignment during LCD production [9, 10]. Furthermore, non-hydrogenated DLCs have a potential application in poly-LED and organic-LED devices [11, 12]. Capacitively coupled rf plasmas of hydrocarbon/H_2 mixtures are frequently used for the deposition of these films. To obtain more insight into the diamond deposition process and so improve film quality and deposition rate(s), an understanding of the chemistry of the gas phase atoms, molecules, radicals and ions is required. Absolute number densities of key ground and excited species and their dependence on operating plasma parameters and spatial location within the reactor provide key information for models of the plasma chemistry [13]. DFG combined with direct absorption spectroscopy and wavelength modulation spectroscopy (WMS) provides an opportunity for sensitive detection of specific species in a plasma and therefore a means to investigate the chemical and physical properties of plasmas and to help unravel the complexity of such systems.

In this paper, we report on the generation of radiation around 3 μm produced by DFG and present measurements on CH_4, C_2H_2, C_2H_4, and C_2H_6 molecules in a rf capacitively coupled CH_4 plasma as a function of plasma input parameters. We employed a multi-track periodically poled PPLN crystal with poling periods between 29 and 32 μm capable of an extended wavelength coverage of 3.1 − 4 μm with the appropriate pump/signal lasers. In the crystal, the laser light of a cw Nd:YAG operating at 1064 nm and one of two DFB diode lasers operating at 1560 nm and 1620 nm were mixed producing light at 3.35 μm and 3.1 μm. The laser light is then directed into the capacitively coupled rf plasma chamber using a multipass configuration to enhance the absorption signal. The signal to noise ratio is further improved by applying wavelength modulation spectroscopy (WMS), which transfers detection to a higher frequency regime to reduce noise.

2. Difference frequency generation

DFG relies upon the non-linear response of a material's induced polarisation when subjected to an intense electric field [14]. More specifically, it is the second order nonlinear optical susceptibility term $\chi^{(2)}$ of the induced polarisation $P(t)$ within the material, that allows the generation of "difference frequency" light. The time-dependent induced polarisation in a material is given by

$$P(t) = \epsilon_0(\chi^{(1)}E_a(t) + \chi^{(2)}E_a(t)^2 + \chi^{(3)}E_a(t)^3 + \ldots), \tag{1}$$

where $E_a(t)$ is the applied electric field, $\chi^{(n)}$ are the non-linear susceptibilities and ϵ_0 is the vacuum permittivity. DFG is one of the three second order nonlinear interactions which generate light through the application of two different electric fields to a material; the others are second harmonic generation (SHG) and sum frequency generation (SFG), which occur simultaneously but with varying degrees of efficiency. In DFG, the ouput radiation or idler radiation, i, is produced by mixing two input radiation sources, the signal, s, and the pump, p. For the DFG process, the conservation of energy provides the following relationship between the pump, signal and idler radiation frequencies: $\omega_p - \omega_s = \omega_i$, where $\omega_p > \omega_s > \omega_i$ by convention.

Since nonlinear processes are phase-sensitive, both pump and signal radiation should have a constant phase relationship in order to maximise the efficiency in generating the idler radiation such that the phase mismatch $\Delta\tilde{k}$ is

$$\Delta\tilde{k} = \tilde{k}_p - \tilde{k}_s - \tilde{k}_i = 0, \tag{2}$$

where $\tilde{k}_p$, $\tilde{k}_s$ and $\tilde{k}_i$ are the wave vectors of the pump, signal and idler radiation, respectively, and $k_j = (n_j\omega_j)/c$, where n_j is the refractive index and c is the speed of light in vacuum. To achieve this the polarisation and focussing of the incident laser beams, the geometry and temperature of the crystal all need to be optimised to ensure a proper phase relationship is maintained between the interacting beams along the propagation direction. Due to chromatic dispersion (the frequency dependence of the refractive index of a material) each wave travels at a different speed through the material and $\Delta\tilde{k}$ becomes non-zero, reducing the efficiency of the nonlinear interaction. Therefore phase matching is required for the incident and produced light rays and this is usually conducted within a birefringent medium in which the refractive index is polarisation dependent. However, in cases where it is not possible to achieve efficient phase matching with birefringent crystals, quasi-phase matching (QPM) can be used; this is achieved by using periodically-poled materials, such as PPLN, where a periodic change in the local polarity of $\chi^{(2)}$ between the layers in the crystal corrects for the phase mismatch. The periodically-poled crystal is made by producing a series of individual crystal 'slices' (each a few tens of microns in thickness) with alternating slices being rotated by 180 °C. This leads to a periodic alternation of the optical axis, changing the sign of $\chi^{(2)}$, allowing efficient generation of the idler radiation. The optimal physical conditions for quasi-phase matching in a periodically-poled crystal are achieved when $\triangle k_{QPM}(T)$ is zero,

$$\Delta k_{QPM}(T) = 2\pi\left(\frac{n_p(T)}{\lambda_p} - \frac{n_s(T)}{\lambda_s} - \frac{n_i(T)}{\lambda_i} - \frac{1}{\Lambda(T)}\right), \tag{3}$$

where λ_p, λ_s and λ_i are the pump, signal and idler wavelengths, respectively, and $\Lambda(T)$ is the temperature-dependent crystal poling period. Finally, $n_p(T)$, $n_s(T)$ and $n_i(T)$ are the temperature- and wavelength-dependent extraordinary refractive indices, respectively, described by the Sellmeier equations for PPLN [15]

$$n_{e,x}^2(\lambda_x, T) = A_1 + B_1 f(T) + \frac{A_2 + B_2 f(T)}{\lambda_x^2 - (A_3 + B_3 f(T))^2} + \frac{A_4 + B_4 f(T)}{\lambda_x^2 - A_5^2} - A_6\lambda_x^2 \tag{4}$$

where λ_x is the wavelength in μm for the i, p and s radiation, and A_z and B_z are the optimised parameters given in table 1. The temperature parameter, $f(T)$, is defined as

$$f(T) = (T - 24.5) \times (T + 570.5), \tag{5}$$

where T is the crystal temperature in °C.

3. Wavelength modulation spectroscopy

In WMS (see for example [16]) the detection frequency is raised to a higher frequency domain where technical noise sources are less likely to interfere with the signal and hence a higher signal-to-noise ratio (SNR) can be achieved compared to conventional absorption spectroscopy. Experimentally, this entails applying a relatively fast sinusoidal modulation to the diode laser current to modulate its wavelength usually in the kHz regime, while slowly scanning the laser to cover the spectral region of interest. The interaction between the absorbing species and the spectrally modulated light leads to the generation of signals at the modulation frequency and various harmonics thereof. Signals can then be demodulated at these frequencies, to obtain higher sensitivity signals, which are however no longer absolute and thus a calibration is needed.

In WMS, the overall instantaneous angular frequency of the electric field of the laser, ω, is the combination of the central laser frequency ω_L which is slowly ramped and traverses the absorption profile and ω_m which is the rapid modulation superimposed on ω_L, with amplitude $\triangle\omega_m$ as described by

$$\omega = \omega_L + \triangle\omega_m \cos(\omega_m t). \tag{6}$$

The interaction between absorbing species and the spectrally modulated light leads to changes in the time-dependent intensity of the modulated radiation which can be expressed as a cosine Fourier series

$$I(\omega_L, t) = \sum_{n=0}^{\infty} A_n(\omega_L)\cos(n\omega_m t), \tag{7}$$

where $A_n(\omega_L)$ (where $n > 0$) are the harmonic components of the series. To record a WMS spectrum the detector signal is demodulated, generally by a lock-in amplifier, where only signals that are at the same frequency and phase as the applied modulation frequency, ω_m, are filtered by the lock-in amplifier for signal averaging.

Assuming that I_0, the baseline signal, is independent of frequency in the absence of an absorber, and by substituting $\omega_m t$ with θ, each individual harmonic component in the presence of a frequency-dependent absorption cross-section, $\sigma(\omega)$, is given by:

$$\begin{aligned} A_n(\omega_L) &= \frac{2}{\pi}\int_0^{\pi} I_0(\omega_L + \triangle\omega_m\cos\theta)\exp[-\sigma(\omega_L + \triangle\omega_m\cos\theta)cl]\cos(n\theta)\,\mathrm{d}\theta \\ &= \frac{2I_0}{\pi}\int_0^{\pi}\exp[-\sigma(\omega_L + \triangle\omega_m\cos\theta)cl]\cos(n\theta)\,\mathrm{d}\theta. \end{aligned} \tag{8}$$

For small absorptions, when $\sigma cl \ll 1$, the expression simplifies to

$$A_n(\omega_L) = \frac{2I_0 cl}{\pi}\int_0^{\pi} -\sigma(\omega_L + \triangle\omega_m\cos\theta)\cos(n\theta)\,\mathrm{d}\theta, \tag{9}$$

hence the magnitude of the harmonic component is directly proportional to the sample concentration, c.

A special case occurs when $\triangle\omega_m$ is much smaller than the halfwidth Γ of the absorption line being probed, resulting in the so-called derivative limit. Using a Taylor series expansion of $\sigma(\omega)$, the expression for this limit is derived from (9) and is given by,

$$A_n(\omega_L) = \frac{I_0 2^{1-n} cL}{n!}\triangle\omega_m^n \left.\frac{\mathrm{d}^n\sigma}{\mathrm{d}\omega^n}\right|_{\omega=\omega_L} \tag{10}$$

In the derivative limit, the magnitude of the n^{th} harmonic component is therefore proportional to the n^{th} derivative of $\sigma(\omega)$. In practical applications the use of $\triangle\omega_m \ll \Gamma$ produces a signal with a small amplitude. The signal size can be increased by applying a larger value of $\triangle\omega_m$, and this value is often chosen to be of the order of Γ to maximise signal amplitude. Even at this magnitude of $\triangle\omega_m$, the signal is qualitatively similar to the n^{th} derivative of the absorption lineshape. In general, it is possible to monitor signals at all harmonics of the modulation frequency, however only the first and second-harmonic signals are commonly used [17].

Although WMS is good for removing technical noise, the WMS spectrum obtained is not self-calibrating, unlike direct absorption. Hence a calibration of the obtained spectra using techniques such as direct absorption spectroscopy or measurements against standard gas mixtures are required in order to determine absolute concentrations. Recent publications report that WMS spectra may be calibrated directly from the residual amplitude modulation (RAM) signal [18, 19].

4. Experimental details

The characteristics of the DFG source have been described previously [3] and so only a brief description follows. The experimental setup used for the work at 3.1 μm is depicted schematically in figure 1. Here, the compact ($3 \times 3 \times 12$ cm) $\sim$ 400 mW Nd:YAG laser (Crystalaser) operating at 1064.73 nm acts as the pump laser and the distributed feedback (DFB) fibre coupled diode laser (Furukawa FOL15DCWD series, $\sim$ 30 mW), tunable between 1618.5 nm and 1622.3 nm, as the signal laser. For the work at 3.35 μm, an equivalent DFB laser (JDSU CQF474708 series) operating between 1559 nm and 1561 nm is used. The resulting laser beam has an instrumental line width of 2 MHz. Wavelength tuning of the system was possible by temperature and current tuning of the diode lasers. A fraction of the DFB laser light is directed onto a spectrum analyser (Melles Griot), with a free spectral range of 2.33 GHz and a finesse of 100, for wavelength calibration. Both beams are co-aligned using a dichroic mirror and focused by lenses prior to the dichroic mirror through a multitrack PPLN crystal in order to generate the difference frequency radiation. The PPLN crystal (HC Photonics, $30 \times 7.9 \times 0.5$ mm) is AR coated for 1064 and 1550 nm and has 7 tracks with poling periods between 29 and 32 μm in 0.5 μm increments of which the 30 μm track was used to generate 3.1 μm radiation and the 30.5 μm track to generate 3.35 μm radiation. The crystal was mounted inside an HC Photonics oven which was optimally aligned using a three-axis micrometer stage and enabled temperature control, via resistive heating, between room temperature and 130 °C, to within 0.1 °C. With the 7 tracks an extensive wavelength range from 3.1 to 4 μm can be covered upon changing the diode laser and tuning the crystal temperature. The relatively low power radiation ($\approx 18\mu$W) around 3 μm was decoupled from the high power diode and YAG radiation using a germanium filter anti-reflection coated for 3 μm; the $\sim$ 3 μm radiation was transmitted whereas the diode and Nd:YAG beams were absorbed or reflected into a beam dump. The $\sim$ 3 μm radiation was collimated using a 50 mm focal length CaF_2 biconvex lens and passed through the plasma chamber.

As discussed previously, the poling period of the PPLN crystal is chosen to optimise phase matching given the pump and signal wavelengths and the properties of the crystal. The refractive index of the crystal varies with temperature and so, with control and stabilisation of crystal temperature, the efficiency of the DFG generation can be optimised for the desired mixing process. In figure 2(a) the measured MIR signal is shown as a function of the crystal temperature for two values of the signal wavelength.

At $\lambda_s = 1620.97$ nm the maximum output power for the MIR radiation is observed at 80 °C. This optimal crystal temperature changes when the DFB laser is scanned across a range of wavelengths due to changes in the QPM conditions inside the PPLN. For example, at $\lambda_s = 1619.5$ nm the optimal temperature is shifted down to 78 °C. The shape of the tuning curves has the characteristic asymmetry associated with focused Gaussian beams and matches the expected tuning curve as shown in ref. [3]. Efficient MIR generation over 15 cm^{-1} was achieved for crystal temperatures of 80 °C and 68.6 °C to produce the 3.1 and 3.35 μm radiation, respectively. In figure 2(b) the measured MIR output versus the wavelength of the diode laser at 1620 nm is plotted for a crystal temperature of 80 °C. This shows that the conversion efficiency changes dramatically as a function of the signal wavelength at a fixed temperature.

Details of the plasma chamber have been previously published [20] and are summarized here. Experiments were carried out in a capacitively-coupled parallel plate rf plasma reactor (Plasma Technology RIE 80) (also shown in figure 1). The rf power at 13.56 MHz was supplied by an analogue power supply (ENI HF 300) to a 170 mm diameter aluminum lower electrode, separated from a similar grounded electrode by 55 mm; the entire electrode assembly of the chamber is water cooled. The power applied varied between 0 and 180 W, with less than 5% reflected power controlled with a matching network. This planar plate configuration is surrounded by a quartz vacuum vessel with an inner diameter of 280 mm, and an alloy box which acts as a Faraday cage to prevent interference of the rf plasma with the electronics of the DFG system. CH_4 gas (BOC 99.5%) entered the chamber via a mass flow controller through a shower-head arrangement imbedded in the upper grounded electrode (typical flow rates $\sim$ 1000 sccm), and were pumped through a 50 mm aperture located below the driven electrode using a roots blower backed by a rotary pump (Edwards EH250 and E2M40, respectively). The working pressure was varied between 0.17 and 2 Torr and was monitored by two capacitance manometers (Ceravac, $0 - 1$ Torr and $0 - 10$ Torr). The chamber was fitted with two side arms with CaF_2 windows, transparent in the 3 μm region, to allow the MIR beam through the plasma chamber. To increase the absorption path length, the beam was passed through the reactor three times by silver mirrors in a multipass configuration. The total path length was 160 cm of which 51 cm was in the plasma region. After multipassing, the light was focused by an off-axis paraboloid mirror, onto a liquid nitrogen cooled InSb detector (New Brunswick).

During direct absorption measurements the laser was scanned over ~ 0.5 cm^{-1} by applying a triangular voltage ramp with at a frequency of 10 Hz to the laser. The 1064 nm beam was modulated using an optical chopper (Bentham, $\sim$ 2.8 kHz) and the detector signal was then demodulated using the lock-in amplifier (Stanford Research Systems, SR510) before being displayed on the oscilloscope (LeCroy WaveSurfer 434); 500 averages were taken for each spectrum. WMS was conducted by applying a low ramping frequency of 2 Hz scanning over ~ 0.5 cm^{-1} to the laser in a similar fashion as for direct absorption measurements. A function generator (TTi TG1304) was used to produce the fast sinusoidal modulation frequency, ω_m, of $\sim$ 22 kHz with a modulation depth, $\triangle\omega_m$, of $\sim$ 257 MHz. The corresponding absorption spectra were obtained by demodulating the detected signal at the desired harmonic using the lock-in-amplifier, before being displayed on the oscilloscope; again 500 averages were taken for each spectrum.

5. Results and discussion

For the measurements of the densities either direct absorption spectroscopy or WMS was used. In figure 3, example spectra of CH_4 taken at 0.17 Torr are shown obtained with both methods without the plasma on. Table 2 contains the details of the transitions probed, such as line position and assignment. In the direct absorption spectrum, the four strong transitions absorbed a considerable amount of the laser intensity and they suffer from line broadening. However, the weaker transitions have an absorption of $< 10\%$ and are not affected in this way. For example, the measured Doppler width of the transition labeled $J = 3$, A_2 is $(9.99 \pm 0.17) \times 10^{-3}$ cm^{-1} which is in relatively good agreement with the theoretical Doppler width of 9.23×10^{-3} cm^{-1} at 298 K, but outside the statistical error quoted. This discrepancy is most likely due to a slight broadening of the line as a result of laser instabilities over the time the spectra were taken (50 seconds). This implies that with direct absorption spectroscopy the temperature of species in the plasma can be determined with a precision of 50 K. The sensitivity of direct absorption spectroscopy can be described by an α_{min} value which is independent of sample and a value of 2×10^{-5} cm^{-1} recorded in 50 seconds was achieved in these experiments determined from the CH_4 data. This corresponds to a minimum detectable density for CH_4 of 1.7×10^{12} cm^{-3}. In figure 3(b), the WMS spectra using $1f$-harmonic detection is shown. Absorption signals detected using WMS always have linewidths that are wider than their corresponding Doppler-limited linewidth due to modulation broadening, but using a fitting routine, the linewidth and therefore temperature can be determined. The magnitude of the absorption is proportional to the species concentration and after calibration the densities can be easily deduced. The main advantage of WMS is that it is less susceptible to baseline variations and noise and here it has typically a 10 times higher signal-to-noise ratio (SNR) than the direct absorption spectroscopy data.

In figures 4(a) – 4(g), WMS spectra are shown for the region 3211.7 – 3218.7 cm^{-1} obtained using $2f$-harmonic detection in a CH_4 plasma; the operating power of the plasma was 180 W and the pressure was 1.57 Torr. In the same figures, spectra are plotted recorded for a reference cell containing 115 Torr of C_2H_2. Although $1f$-harmonic detection gave larger signal amplitudes, $2f$-harmonic detection was used throughout these experiments to reduce baseline variation. Analysis of the spectra presented in figures 4(a) to 4(f) provides information on several vibrationally excited species in C_2H_2. Transitions from the ground state and numerous transitions from hot bands were observed: various transitions from 22 different vibrational bands were successfully assigned by comparing the obtained spectra to Rinsland's study [21] on C_2H_2 in the 3 μm region. The assignments are shown in the spectra and the vibrational bands they belong to are listed in table 3. Part of the unassigned transitions in the plasma spectra must be C_2H_2 transitions as they are also observed in the gas cell. The other unassigned transitions could be from C_xH_y molecules, or radicals like CH_3 and C_2H. The $2f$-harmonic detection sensitivity is 2×10^{-6} cm^{-1} recorded in 250 seconds corresponds to a minimum detectable density of 10^{12} cm^{-3} when using integrated transition cross sections of $\sim 10^{-22}$ cm^2 cm^{-1} molecule^{-1}, typical of hydrocarbon molecules, and indicates the potential of this methodology for probing radical species such as CH_3, which densities are reported to be of this order of magnitude [22, 23].

C_2H_2 has two low lying vibrational states which are significantly populated at room temperature (also probed and relevant transitions shown in the figures) corresponding to the ν_4 and ν_5 bending modes at 612 cm^{-1} and at 730 cm^{-1}, respectively. Taking the spectrum recorded at room temperature with a C_2H_2 cell containing 115 Torr of gas as a benchmark for the relative heights of absorption lines, and adjusting the observed heights for a change in rotational temperature from 298 to 400 K (see further on), an estimate of the degree of vibrational excitation with the plasma on can be obtained. It should be noted that the an apparent increase in vibrational population due to a temperature increase to 400 K has not been included here, as quite often in plasma systems the vibrational and rotational modes are decoupled. The spectra indicate that populations in the ν_4 and ν_5 levels are being depleted with respect to the ground state, but with populations in the $2\nu_4$ and $2\nu_5$ levels enhanced, pointing towards a non-Boltzmann vibrational distribution. Further work is required on other higher lying vibrational states in order to determine the vibrational energy distribution, and whether or not it is perhaps well described by a two temperature Boltzmann function.

According to the Beer-Lambert law, the absorption signal due to a species with a particular density is proportional to the cross-section of that species. The cross-sections relating the absorption to the density of a species are temperature dependent because they depend upon the temperature dependent populations of individual quantum states. Hence knowledge of the plasma temperature is needed for total density measurements. By measuring the rotational temperature, T_{rot}, of the C_2H_2 in the plasma, total densities for a particular vibrational level can be calculated assuming that the rotational populations are described by a Boltzmann distribution for all the species. The rotational temperature is obtained by taking the ratio of the integrated absorptions of two transitions that originate from the same lower vibrational state as this cancels the dependence of the line intensity on the total internal partition function, $Q(T)$, and the ratio becomes temperature-dependent only. In order to increase the SNR, strong C_2H_2 transitions in the region $3212 - 3218$ cm^{-1} were measured with direct absorption spectroscopy; their line positions and assignments are given in table 4. In the extraction of T_{rot} as a function of plasma power and pressure, the average of the ratios of P27/P31 and P31/P26 were determined. Of the transitions that are in the accessed spectral region, these two sets of transitions have intensity ratios that are most sensitive to a change in T_{rot} (a factor of 1.3 over 100 K) because they involve rotational levels that are furthest apart (in energy) and hence have the largest rotational population differences for a given set of conditions. The measured T_{rot} was essentially invariant to the change in plasma pressure or rf power within the experimental error. Thus, an averaged value of $T_{rot} = 400 \pm 55$ K was assumed and the rotational, vibrational and translation temperature were all assumed to be equal in order to calculate the integrated cross-sections for the observed transitions. These assumptions probably result in an underestimation of the densities as the C_2H_2 spectra indicate a non-Boltzmann vibrational distribution for C_2H_2. All of the measurements are also spatial averages and assume a uniform density distribution and temperature distribution through the chamber. In tables 4 − 6, the details of the transitions probed such as line position, the integrated cross section at 400 K and the assignments obtained from the HITRAN 2008 database [24] are given. At the reported plasma temperature, the absorption cross-sections of C_2H_4 in the accessible wavelength range are at least an order of magnitude smaller than those of C_2H_2. Due to its low detection limit, we were not able to detect C_2H_4 by direct absorption spectroscopy under all the conditions investigated. Hence the C_2H_4 density was determined from WMS spectra. Since the peak height of an absorption profile in a WMS spectrum is proportional to the density of the absorbing species, the ratio of peak heights between transitions of C_2H_4 and C_2H_2 allows the C_2H_4 density to be estimated, given that the ratio is corrected for the difference in the absorption cross-sections of the two species, and the WMS data on C_2H_2 have been calibrated from direct absorption spectroscopy measurements. The C_2H_6 densities could be obtained by direct absorption spectroscopy under all experimental conditions.

The densities reported are the averaged densities determined using the transitions listed in the tables 4 – 6 for C_2H_2, C_2H_4, and C_2H_6. The obtained densities of C_2H_2, C_2H_4, and C_2H_6 were insensitive to changes in plasma pressure and rf power within the experimental error and were around $7.9 \pm 0.3 \times 10^{14}$ cm^{-3}, $9.5 \pm 1.5 \times 10^{14}$ cm^{-3}, and $7.9 \pm 2.2 \times 10^{14}$ cm^{-3} for C_2H_2, C_2H_4, and C_2H_6, respectively. The uncertainty in the temperature and thus integrated cross section results in an error of 20% for C_2H_2, 10% for C_2H_4, and 32% for C_2H_6. We note that the C_2H_2 density was found to vary between 7.8×10^{14} cm^{-3} and 8.4×10^{14} cm^{-3} for repeated measurements on different days under the same conditions (0.84 Torr and 180 W). The recorded densities hence show a very good agreement between measurements, despite the large possible error estimated. These densities are of the same order of magnitude as observed in rf CH_4 plasmas assuming a Boltzmann density distribution over the rotational and vibrational states [22, 23].

We also determined the CH_4 depletion under the conditions investigated. From the spectra, we determined the rotational temperature of the CH_4 molecules in the plasma to be 330 ± 25 K and used this temperature to calculate the integrated cross-sections for the transitions assuming a Boltzmann density distribution. In the process of calculating the CH_4 density, it has to be remembered that the plasma is confined between the electrodes and that the plasma region is only one third of the total optical pathlength. Therefore, a line-of-sight radiation beam measures the averaged properties of CH_4, and the obtained T_{rot} is thus the averaged rotational temperature of a third of CH_4 at plasma temperature (400 K) and the rest being at presumably a lower temperature resulting in 330 K. The rotational temperatures of 400 K for species in the center of the chamber and 330 K for CH_4 molecules is in agreement with previous measured temperatures in rf CH_4 plasmas [23, 25]. In table 2, the details of the transitions probed such as line position, the integrated cross section at 330 K and the assignments obtained from the HITRAN 2008 database [24] are given. The deduced CH_4 depletion is presented in figures 5(a) and 5(b) for varying CH_4 pressure and plasma power. The depletion of CH_4 increased from 23% at 40 W to 40% at 180 W, and increased to 56% as the pressure decreases to 0.45 Torr. This conforms to the intuitive notion that an increase in the rf power driving the plasma increases both the electron temperature and number density and therefore more dissociation takes place in the plasma (as is always found in these systems). The C_2H_2, C_2H_4, and C_2H_6 densities are however relatively insensitive to the plasma conditions compared with the methane loss resulting in a discrepancy in the carbon balance. The missing carbon atoms could be related to the deposition of carbon films on the walls of the plasma chamber but we note however that it is impossible to deduce exactly the chemical balance of the plasma without knowledge of the vibrational population distribution.

6. Conclusion

This paper demonstrates the practicality of a compact solid-state laser based DFG system as a tool for probing hydrocarbon based plasmas. The production of mid-infrared radiation has been successfully achieved by combining 1064 nm radiation from a cw Nd:YAG laser with 1560/1620 nm radiation from distributed feedback (DFB) fibre coupled diode lasers in a PPLN crystal. The resultant 18 μW of radiation around 3.2 μm has been used to probe a rf capacitively couple CH_4 plasma for a matrix of conditions, varying power (< 180 W) and pressure (< 1 Torr) in both direct absorption spectroscopy and WMS experiments to achieve relatively high sensitivities while retaining accurate spectral information in the form of linewidths. An α_{min} value of 2×10^{-5} cm^{-1} was achieved for direct absorption spectroscopy which corresponds to a minimum detectable density for CH_4 of 1.7×10^{12} cm^{-3}. The conversion of CH_4 to other species was determined by measuring the densities of C_2H_2, C_2H_4, and C_2H_6 which were respectively around $7.9 \pm 0.3 \times 10^{14}$ cm^{-3}, $9.5 \pm 1.5 \times 10^{14}$ cm^{-3}, and $7.9 \pm 2.2 \times 10^{14}$ cm^{-3}. Finally, the depletion of CH_4 was measured to increase from 23% at 40 W to 40% at 180 W at a pressure of 0.84 Torr, and the depletion increased to 56% as the pressure decreases to 0.45 Torr.

Acknowledgments

The authors would like to thank the EPSRC for the award of an Advanced Research Fellowship (R.P.)

References

[1] J Röpcke, G Lombardi, A Rousseau, and P B Davies. *Plasma Sources Sci. Technol.*, 15:S148, 2006.

[2] R F Curl, F Capasso, C Gmachl, A A Kosterev, B McManus, R Lewicki, M Pusharsky, G Wysocki, and F K Tittel. *Chem. Phys. Lett.*, 487:1, 2010.

[3] H Y Clark, L Corner, W Denzer, G Hancock, A Hutchinson, M Islam, R Peverall, and G A D Ritchie. *Chem. Phys. Lett.*, 399:102, 2004.

[4] W Chen, J Cousin, E Poullet, J Burie, D Boucher, X Gao, M W Sigrist, and F K Tittel. *C. R. Phys.*, 8:1129, 2007.

[5] O Tadanaga, T Yanagawa, Y Nishida, H Miyazawa, k Magari, M Asobe, and H Suzuki. *Appl. Phys. Lett.*, 88:061101, 2006.

[6] L H Deng, X M Gao, Z S Cao, W D Chen, Y Q Yuan, W J Zhang, and Z B Gong. *Opt. Commun.*, 281:1686, 2008.

[7] G D'Amico, G Pesce, G Rusciano, and A Sasso. *Opt. Laser. Eng.*, 37:481, 2002.

[8] J Robertson. *Mater. Sci. Eng.*, R37:129, 2002.

[9] P Chaudhari, J Lacey, J Doyle, E. Galligan, S-C A Lien, A Callegari, G Hougham, N D Lang, P S Andry, R John, K-H Yang, M Lu, C Cai, J Speidell, S Purushothaman, J Ritsko, M Samant, J Stöhr, Y Nakagawa, Y Katoh, Y Saitoh, K Sakai, H Satoh, S Odahara, H Nakano, J Nakagaki, and Y Shiota. *Nature*, 411:56, 2001.

[10] J Stöhr, M G Samant, J Lüning, A C Callegari, P Chaudhari, J P Doyle, J A Lacey, S A Lien, S Purushothaman, and J L Speidell. *Science*, 292:2299, 2001.

[11] R Reyes, C Legnani, P M Ribeiro pinto, M Cremona, P J G de Araújo, and C A Achete. *Appl. Phys. Lett.*, 82:4017, 2003.

[12] K Lmimouni, C Legrand, C Dufour, A Chapoton, and C Belouet. *Appl. Phys. Lett.*, 78:2437, 2001.

[13] J E Butler, Y A Mankelevich, A Cheesman, J Ma, and M N R Ashfold. *J. Phys.: Condens. Matter*, 21:364201, 2009.

[14] R W Boyd. *Nonlinear Optics.* Academic Press, San Diego, 2nd edition, 2003.

[15] D H Jundt. *Opt. Lett.*, 22:1553, 1997.

[16] J M Supplee, E A Whittaker, and W Lenth. *Appl. Opt.*, 33:6294, 1994.

[17] A Hutchinson. *Diode laser studies of trace species and their reactions.* Dphil thesis, University of Oxford, 2006.

[18] K Duffin, A J McGettrick, W Johnstone, G Stewart, and D G Moodie. *J. Lightwave Technol.*, 25:3114, 2007.

[19] A J McGettrick, K Duffin, W Johnstone, G Stewart, and D G Moodie. *J. Lightwave Technol.*, 26:432, 2008.

[20] G Hancock and J P Sucksmith. *J. Vac. Sci. Technol. A*, 20:270, 2002.

[21] C P Rinsland, A Baldacci, and K Narahari Rao. *Astrophys. J. Suppl. Ser.*, 49:487, 1982.

[22] P B Davies and P M Martineau. *Appl. Phys. Lett.*, 57:237, 1990.

[23] P B Davies and P M Martineau. *J. Appl. Phys.*, 71:6125, 1992.

[24] L S Rothman, I E Gordon, A Barbe, D Chris Benner, P F Bernath, M Birk, V Boudon, L R Brown, A Campargue, J-P Champion, K Chance, L H Coudert, V Dana, V M Devi, S Fally, J-M Flaud, R R Gamache, A Goldman, D Jacquemart, I Kleiner, N Lacome, W J Lafferty, J-Y Mandin, S T Massie, S N Mikhailenko, C E Miller, N Moazzen-Ahmadi, O V Naumenko, A V Nikitin, J Orphal, V I Perevalov, A Perrin, A Predoi-Cross, C P Rinsland, M Rotger, M Šimečiková, M A H Smith, K Sung, S A Tashkun, J Tennyson, R A Toth, A C Vandaele, and J Vander Auwera. *J. Quant. Spectrosc. Radiat. Transfer*, 110:533, 2009.

[25] C Busch, I Möller, and H Soltwisch. *Plasma Sources Sci. Technol.*, 10:250, 2001.

List of figure captions:

(1) Schematic of the DFG experimental setup.

(2) (a) Experimentally measured tuning curves for two signal wavelengths, 1620.97 nm (■) and 1619.52 nm (○), as a function of crystal temperature. (b) The measured MIR signal as a function of the wavelength of the diode laser at 1620 nm at a temperature of 80 °C.

(3) (a) Direct absorption spectrum and (b) Wavelength modulation spectrum of 0.17 Torr of CH_4 without the plasma on. In the direct absorption spectrum, the four strong transitions absorbed a considerable amount of the laser intensity and they suffer from line broadening. The details of the transitions probed are given in table 2.

(4) WMS spectra of C_2H_2 in the region $3211.7 - 3218.7\ \mathrm{cm}^{-1}$ as measured in a reference cell of 115 Torr of C_2H_2 (top) and of the CH_4 plasma (bottom) using $2f$-harmonic detection; the operating power of the plasma was 180 W and the pressure was 1.57 Torr. Marked in the spectra are transitions which could be assigned in both the 115 Torr cell and in the plasma and the vibrational bands they belong to are listed in table 3. The other lines observed are not assigned, but part of them are from C_2H_2 transitions as they are observed in both spectra. The other unassigned transitions could be from C_xH_y molecules, or radicals like CH_3 and C_2H.

(5) The depletion of CH_4 as a function of (a) CH_4 pressure at a power of 180 W and (b) plasma power at a pressure of 0.84 Torr.

Table 1. The A_z and B_z parameters of the Sellmeier equation for PPLN [15].

z	1	2	3	4	5	6
A	5.35583	0.100473	0.20692	100	11.34927	1.5334×10^{-2}
B	4.629×10^{-7}	3.862×10^{-8}	-0.89×10^{-8}	2.657×10^{-5}		

Table 2. Details of the transitions of the ν_3 asymmetric stretch mode of CH_4 , where J is the rotational quantum number and C gives the symmetry [24].

Line position (cm^{-1})	Integrated cross-section, $T = 330$ K (cm^2 cm^{-1} $molecule^{-1}$)	Transition				
		J’	C’	←	J”	C”
2978.650460	6.375×10^{-20}	3	F_1		4	F_2
2978.692630	1.040×10^{-21}	2	A_1		3	A_2
2978.808300	6.221×10^{-22}	2	F_1		3	F_2
2978.848048	4.277×10^{-20}	3	E		4	E
2978.893260	6.239×10^{-22}	2	F_2		3	F_1
2978.919811	6.407×10^{-20}	3	F_2		4	F_1
2978.956100	4.468×10^{-22}	9	F_1		8	F_2
2979.011290	1.070×10^{-19}	3	A_2		4	A_1

Table 3. Assignments of the C_2H_2 bands in the 3 μm region observed in our WMS spectra [21].

Label	Upper Level	Lower Level
$^{12}C_2H_2$		
I	$010(11)^0_+(\Sigma_u^+)$	$0000^00^0(\Sigma_g^+)$
II	$010(21)^1(\mathrm{II})(\Pi_u)$	$0001^10^0(\Pi_g)$
III	$010(12)^1(\mathrm{II})(\Pi_g)$	$0000^01^1(\Pi_u)$
IV	$010(31)^0_+(\mathrm{II})(\Sigma_u^+)$	$0002^00^0(\Sigma_g^+)$
V	$010(31)^2(\mathrm{II})(\Delta_u)$	$0002^20^0(\Delta_g)$
VI	$010(22)^0_-(\Sigma_g^-)$	$000(11)^0_-(\Sigma_u^-)$
VII	$010(22)^2(\mathrm{II})(\Delta_g)$	$000(11)^2(\Delta_u)$
VIII	$010(13)^2(\mathrm{II})(\Delta_u)$	$0000^02^2(\Delta_g)$
IX	$0010^00^0(\Sigma_u^+)$	$0000^00^0(\Sigma_g^+)$
X	$0011^10^0(\Pi_u)$	$0001^10^0(\Pi_g)$
XI	$0010^01^1(\Pi_g)$	$0000^01^1(\Pi_u)$
XII	$0012^00^0(\Sigma_u^+)$	$0002^00^0(\Sigma_g^+)$
XIII	$0012^20^0(\Delta_u)$	$0002^20^0(\Delta_g)$
XIV	$001(11)^0_+(\Sigma_g^+)$	$000(11)^0_+(\Sigma_u^+)$
XV	$001(11)^2(\Delta_g)$	$000(11)^2(\Delta_u)$
XVI	$0010^02^0(\Sigma_u^+)$	$0000^02^0(\Sigma_g^+)$
XVII	$0010^02^2(\Delta_u)$	$0000^02^2(\Delta_g)$
XVIII	$1001^10^0(\Pi_g)$	$0000^01^1(\Pi_u)$
$^{12}C^{13}CH_2$		
XIX	$0010^00^0(\Sigma^+)$	$0000^00^0(\Sigma^+)$
XX	$0011^10^0(\Pi)$	$0001^10^0(\Pi)$
XXI	$0010^01^1(\Pi)$	$0000^01^1(\Pi)$
XXII	$010(11)^0_+(\Sigma^+)$	$0000^00^0(\Sigma^+)$

Table 4. Details of the C_2H_2 transitions [24].

Line position (cm^{-1})	Integrated cross-section, $T = 400$ K ($cm^2\ cm^{-1}$ molecule^{-1})	Upper vibrational level	Lower vibrational level	Transition
3212.640735	8.82×10^{-21}	$010(11)^0_+(\Sigma_u^+)$	$0000^00^0(\Sigma_g^+)$	P28e
3215.253045	3.21×10^{-20}	$010(11)^0_+(\Sigma_u^+)$	$0000^00^0(\Sigma_g^+)$	P27e
3217.066339	9.69×10^{-21}	$0010^00^0(\Sigma_u^+)$	$0000^00^0(\Sigma_g^+)$	P31e
3217.853528	1.29×10^{-20}	$010(11)^0_+(\Sigma_u^+)$	$0000^00^0(\Sigma_g^+)$	P26e

Table 5. Details of the transitions of the ν_9 asymmetric CH_2 stretch mode of C_2H_4, where J, K_a and K_c are the rotational quantum numbers [24].

Line position (cm^{-1})	Integrated cross-section, $T = 400$ K ($\mathrm{cm}^2\ \mathrm{cm}^{-1}$ molecule^{-1})	Transition						
		J'	K$_a$'	K$_c$'	←	J"	K$_a$"	K$_c$"
3217.359364	8.17×10^{-22}	14	12	3		13	11	2
3217.359364	8.17×10^{-22}	14	12	2		13	11	3
3217.585582	2.735×10^{-22}	27	9	18		26	8	19
3217.585582	6.381×10^{-22}	27	9	19		26	8	18

Table 6. Details of the transitions of the ν_7 band of C_2H_6 [24].

Line position (cm^{-1})	Integrated cross-section, $T = 400$ K (cm^2 cm^{-1} $molecule^{-1}$)	Transition						
		J'	K'	C'	←	J"	K"	C"
2977.6969	9.73×10^{-22}	16	2	E4		15	0	E4
2977.7077	1.62×10^{-21}	16	2	A4		15	0	A2
2977.8456	2.14×10^{-21}	16	2	Eu		15	1	Eg

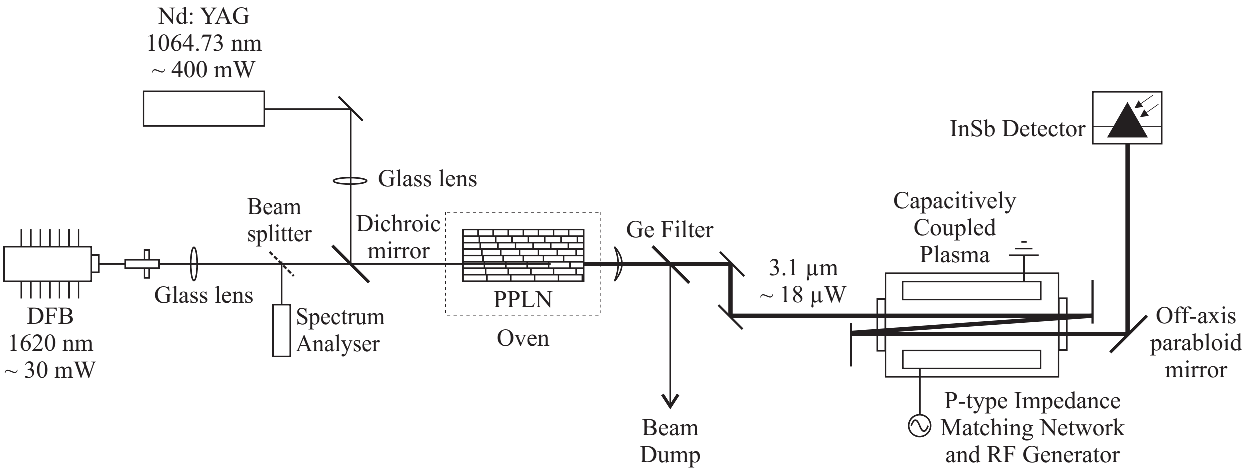

Figure 1. van Helden et al.

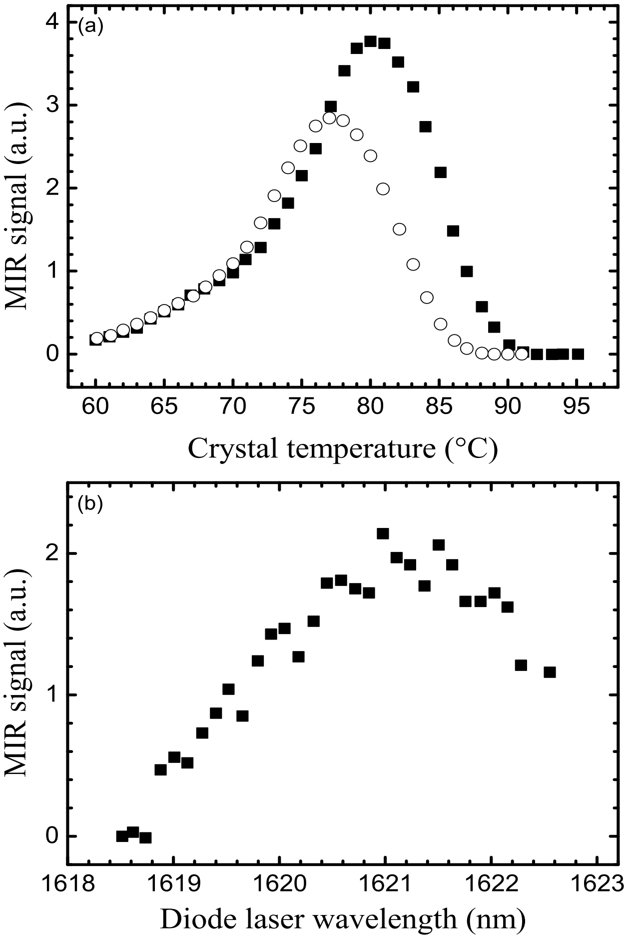

Figure 2. van Helden et al.

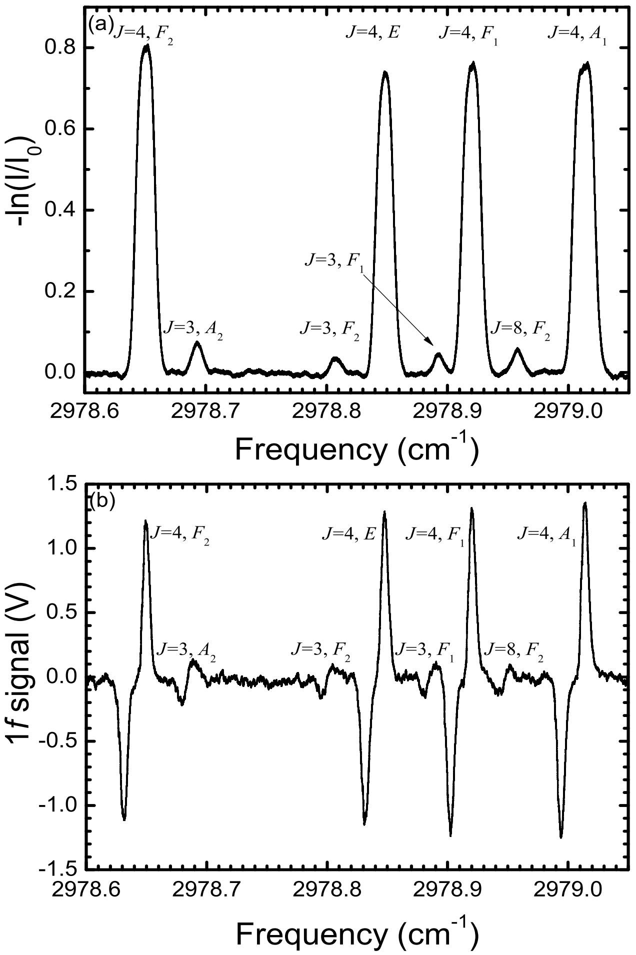

Figure 3. van Helden et al.

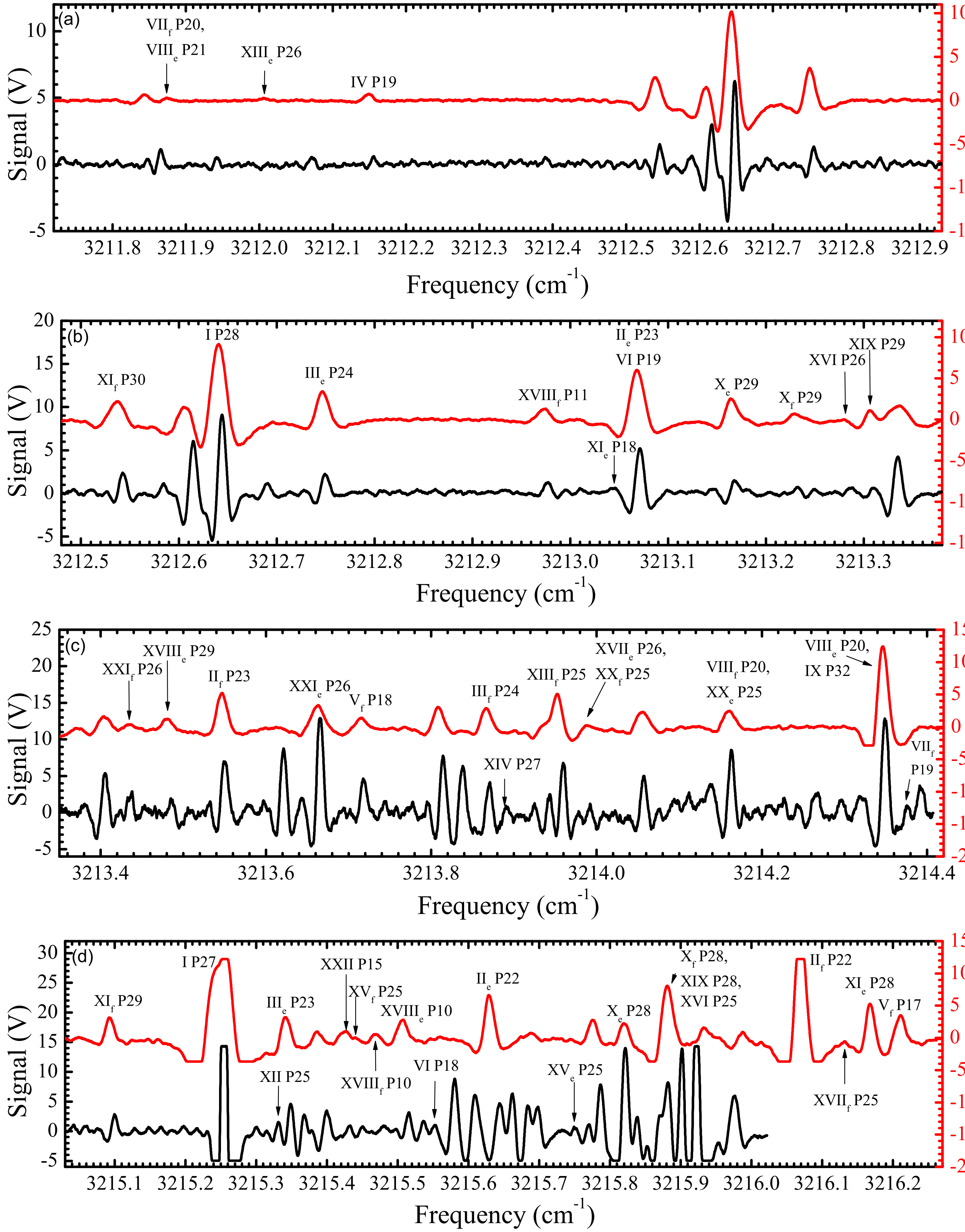
(a)
VII$_f$ P20,
VIII$_e$ P21
XIII$_e$ P26
IV P19
Signal (V)
10
5
0
-5
-10
-15
3211.8
3211.9
3212.0
3212.1
3212.2
3212.3
3212.4
3212.5
3212.6
3212.7
3212.8
3212.9
Frequency (cm^{-1})
(b)
XI$_f$ P30
I P28
III$_e$ P24
XVIII$_f$ P11
II$_e$ P23
VI P19
XI$_e$ P18
X$_e$ P29
X$_f$ P29
XVI P26
XIX P29
Signal (V)
20
15
10
5
0
-5
-10
-15
3212.5
3212.6
3212.7
3212.8
3212.9
3213.0
3213.1
3213.2
3213.3
Frequency (cm^{-1})
(c)
XXI$_f$ P26
XVIII$_e$ P29
II$_f$ P23
XXI$_e$ P26
V$_f$ P18
III$_f$ P24
XIII$_f$ P25
XIV P27
XVII$_e$ P26,
XX$_f$ P25
VIII$_f$ P20,
XX$_e$ P25
VIII$_e$ P20,
IX P32
VII$_f$
P19
Signal (V)
25
20
15
10
5
0
-5
-10
-15
-20
3213.4
3213.6
3213.8
3214.0
3214.2
3214.4
Frequency (cm^{-1})
(d)
XI$_f$ P29
I P27
XII P25
III$_e$ P23
XXII P15
XV$_f$ P25
XVIII$_f$ P10
XVIII$_e$ P10
VI P18
II$_e$ P22
XV$_e$ P25
X$_e$ P28
X$_f$ P28,
XIX P28,
XVI P25
II$_f$ P22
XVII$_f$ P25
XI$_e$ P28
V$_f$ P17
Signal (V)
30
25
20
15
10
5
0
-5
-10
-15
-20
3215.1
3215.2
3215.3
3215.4
3215.5
3215.6
3215.7
3215.8
3215.9
3216.0
3216.1
3216.2
Frequency (cm^{-1})

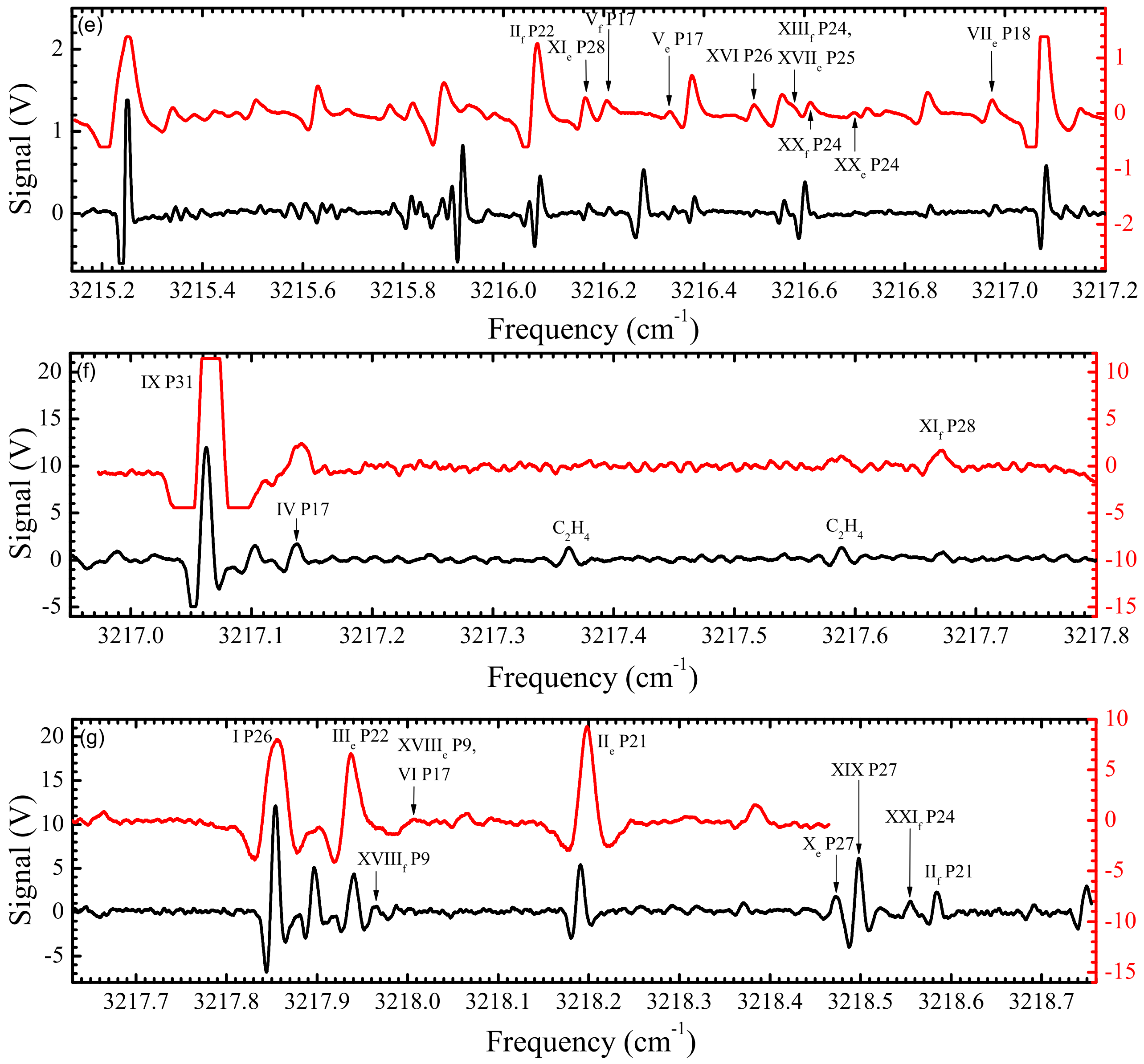

Figure 4. van Helden et al.

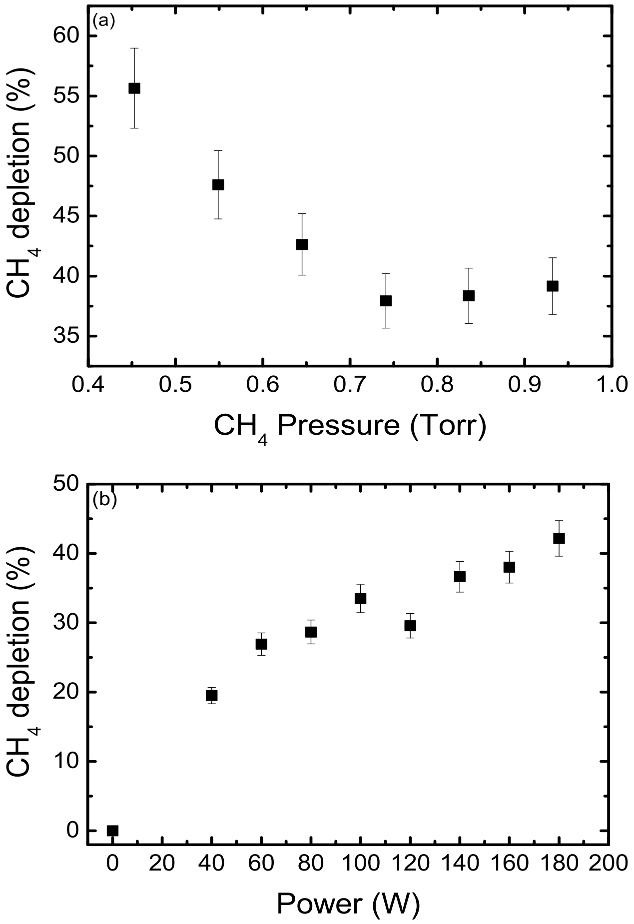

Figure 5. van Helden et al.